LAWRENCE
LIVERMORE
NATIONAL
LABORATORY

LLNL-JRNL-823443

Microscale Strain and Phase Evolution of Additively Manufactured Ti-6Al-4V

C. Andrews, C. Basgul, T. Heo, R. Shi, M. J. Matthews, S. Kurtz, M. L. Taheri

June 11, 2021

Materials Science & Engineering A

Disclaimer

Title: Interplay of strain and phase evolution of laser powder bed fusion Ti-6Al-4V

C. Andrews[1], T.W. Heo[2], R. Shi[2], C. Başgül[3], S. Kurtz[4], M.J. Matthews[2], and M.L. Taheri[1]
1. Department of Materials Science and Engineering, Johns Hopkins University, Baltimore, MD
2. Materials Science Division, Lawrence Livermore National Laboratory, Livermore, CA 94550, USA
3. School of Biomedical Engineering, Science and Health Systems, Drexel University, Philadelphia, PA
4. Biomedical Engineering, Exponent Engineering and Science Consulting, Philadelphia, PA

Abstract

While additive manufacturing (AM) provides a method of producing geometrically complex and highly detailed structures, the generation of residual strain in AM processes like laser powder bed fusion (L-PBF) can negatively impact performance-enabling properties. In applications such as orthopedic implants, specific performance windows require optimized microstructures in order to obtain desirable properties from multi-phase alloys like Ti-6Al-4V. This research aims to quantify the microscale origins of strain in L-PBF manufactured Ti-6Al-4V by understanding how strain is distributed at the grain and sub-grain scale, the interplay between phase evolution and strain, and examining post-processing strain relief strategies to control these features. Model spinal cage implants were manufactured from Ti-6Al-4V powder via L-PBF and then subjected to strain relieving heat treatment cycles above and below the Ti-6Al-4V β transus as a function of time and cooling rate. Residual strain was then studied via high resolution electron backscatter diffraction (HR-EBSD), and 2D strain maps with sub-micron resolution were generated for each post-processing state. It was found that macroscale thermal strains decreased with heat treatment time, but additional contributions from phase stabilizing residual strains retained primarily in the α' grains as lattice distortive strain remained. Additionally, the retention of β phase significantly changed the strain and dislocation distribution while reducing overall residual strain. These results were validated and reinforced with 3D mesoscopic micromechanical modeling of strain behavior across simulated microstructures, confirming that the local lattice dilation of α' martensite is a primary contributor of microscale strain generation and retention in L-PBF Ti-6Al-4V.

Keywords: titanium alloy, residual strains, lattice strains, additive manufacturing, electron backscatter diffraction (EBSD)

1. Introduction

Laser powder bed fusion (L-PBF) is a popular method for metal additive manufacturing (AM) that utilizes a high-power laser (or lasers) to produce a three dimensional part by successively melting layers of metal powder to freely form complex geometries with near net shape production. [1] This method has shown promise for manufacturing traditionally hard-to-machine alloys, such as Ti-6Al-4V, where reliance on forging, casting, rolling, and subsequent machining results in high lead times, material waste, and manufacturing costs. [2] Additionally, the poor thermal conductivity [3] and the propensity of Ti-6Al-4V to strain harden when worked [4] introduces more complexity towards its manufacture. L-PBF being a more flexible, tooling free, manufacturing method provides a route to produce patient-specific implants with fine feature sizes from biocompatible alloys like Ti-6Al-4V, which is an alloy of particular interest to the biomedical industry due to its high biocompatibility, fatigue resistance, and corrosion resistance. [5]–[7] In fact, these excellent properties qualify this alloy as one of the only alloys available to readily bio-integrate and ossify. [8], [9] Thus for these biomedical applications, L-PBF shows potential for enabling more complex, topologically controlled, and personalized orthopedics with the ability to alleviate issues related to stress shielding such as bone loss and reduce implant revision surgery. [10]–[14]

L-PBF is the most widely used and studied AM method, with 31% of all AM papers published in 2019 focusing on the method, [15] but in comparison to other popular methods like binder jet fusion or freeform electron beam fabrication, it features higher levels of residual strain within a given part. [16] In L-PBF, the laser spot moves at ~1 m/s over the powder surface to produce a localized melt pool, which rapidly cools as the laser moves across the surface to produce a solid layer before being re-coated with a new layer of powder. [17] This highly localized melting process and small material interaction region give rise to large thermal gradients with very high cooling rates of up to 10^6 K/s. [18], [19] This cyclical process of rapid heating and cooling can produce multiscale and spatially inhomogeneous residual strain in the part, the magnitude of which has been shown to vary at the bulk scale with part geometry, size, and microstructure. [20]–[23] This has broad implications for the performance of L-PBF parts leading to build failure, geometric distortion, and premature part failure. [21], [24]–[26] With respect to Ti-6Al-4V and its use as an aerospace and biomedical alloy, it has been demonstrated that strain buildup can negatively impact fatigue and strength properties, which are critical to the acceptance of a part through Federal Aviation Administration and Food and Drug Administration guidelines. [17], [27]–[29] Strains can be generated not just by thermal tension-compression asymmetries, but through phase and orientation mismatch at the microscale as well. In casting or more slowly cooled manufacturing processes, Ti-6Al-4V forms a stable (α+β) dual-phase microstructure with the V stabilizing the *bcc* β phase and the Al stabilizing the *hcp* α phase. The rapid cooling environment during the L-PBF process, however, does not allow sufficient time for solute diffusion to form this α+β two-phase structure, and results is in a diffusionless transformation to a metastable α’ phase microstructure. [17], [30]–[33] The metastable α’ martensite has been shown to have high dislocation density, leading to high hardness and low ductility due to dislocation strengthening and substitutional solution strengthening. [34]–[37] This presents a multiscale problem of strain generation, retention, and measurement, where thermal tension-compression strains can manifest over the length scale of the part while coherency strains between phases, orientation mismatch, and strain fields surrounding dislocation structures and pile-ups manifest and the microscale. [38], [39]

With regard to the effects of heat treatment on both microstructure and associated bulk mechanical properties of Ti-6Al-4V, it has been shown that when annealing below the β transus, the primary effects are α’ lath coarsening and decomposition into α leading to a decrease in ultimate tensile strength (UTS), but an increase in ductility. [40]–[42] Annealing above the β transus produces the more ductile (α+β) dual-phase microstructure and washes out any L-PBF processing footprint, which is certainly dependent on time, temperature, and cooling rate as well. [43]–[45] For further reading, relevant work and comprehensive discussions on the heat treatment of AM Ti-6Al-4V can be found in Kim *et al.* and Vrancken *et al.* [46], [47]

L-PBF is able to shape and influence materials at the microscale, and in order to understand the feedback loop of process and properties in multiphase materials one must quantitatively measure and model the interplay of microstructure, phase, and strain across the scales where they manifest. Plastic strain in Ti-6Al-4V can be localized via phases and microstructural texture, [48] and *in-situ* high energy X-ray diffraction microscopy (HEDM) of Ti-6Al-4V has shown strain concentration at phase interfaces; [49] both indicating that strains at the microscale are driven by localized phase concentrations and their distributions in the microstructure. Thus, concentrations of phases which promote strain could form localized strain concentrations and play critical roles in determining material performance and failure mechanisms. For Ti-6Al-4V, the α → β phase decomposition as a function of heat treatment has been examined with HEDM [42], and the decomposition of α’ martensite phases formed via L-PBF has been shown to decrease bulk tensile strength while increasing ductility [40].

Phase and strain also interplay in other multi-phase alloy systems, such as IN718, where the expression of secondary phases allowed for strain partitioning, and it was found that by altering the microstructure and phase topology via heat treatment new deformation mechanics and increased strength is achieved. [50] Although it has been verified that the rapid cooling of L-PBF can create a highly strained microstructure, more foundational and systematic investigation has yet to quantify and deconvolute the strains driven by microscale effects, phase localized strains, and their contribution to overall residual strain generation and relaxation.

L-PBF usually forms metastable martensitic microstructures due to the rapid cooling rate which is coupled with thermally induced strain from tension-compression asymmetries at the part-scale. Accordingly, phase microstructure-related strains and thermal asymmetric strains coexist and manifest differently across scale, and to what degree these strains are interweaved remains an open question. Therefore, understanding the strain generation/relaxation mechanisms and deconvoluting the coupled strain factors that appear at the microscale in these materials is critical towards engineering strain free L-PBF microstructures and/or controlling strain formation at the microstructure level. This study employs high-resolution electron backscatter diffraction (HR-EBSD) to experimentally quantify the inter- and intragranular residual strain relaxation as a function of annealing and associated phase morphology; comparing and validating these microscale observations with micromechanical modeling of dual phase microstructures of L-PBF Ti-6Al-4V. The HR-EBSD method of cross-correlation of shifts between ROI within a Kikuchi pattern allows for the measurement of elastic strain from local changes in interplanar angles between electron diffraction patterns, and maintains a strain sensitivity of $\sim 10^4$ with spatial resolution that can easily probe the sub-micron regime. [51] This method has been validated in SiGe alloys and shows agreement with finite-element elastic models [52], and with NIST researchers comparing strain measurements from cross-correlative HR-EBSD to micro-Raman and atomic force microscopy (AFM) in notched Si and showing agreement between the methods and stress profiles consistent with the Eshelby analysis of the inverse-square power law. [53], [54] Furthermore, in steels the method has successfully mapped the precise contributions from, and strain accommodation within, the austinite phase in response to surrounding lenticular/lath martensite lattice strains. [55] HR-EBSD strain analysis has shown utility in analyzing the interplay of geometrically necessary dislocation (GND) density, microstructure, and strain across different AM processes, showing that the higher energy deposition rates of L-PBF result in higher elastic strain which trends with GND density and agrees with cooling rate studies done via X-ray diffraction. [16], [56]

We argue that the Ti-6Al-4V martensite formed via L-PBF will be intragranularly strained due to the lattice distortive mechanisms involving vanadium being substitutionally pinned within the martensite, a wholly different mechanism than thermally driven tension-compression asymmetry, and that these phase-related strains are relaxed differently and contribute significantly to the overall strain distribution within the material. Following the dissolution of the martensite and formation of an (α+β) microstructure, significantly lower strains were observed in both simulated and experimentally observed microstructures as a function of their phase morphology. The α’ phase was found to contain higher levels of residual strain relative to the surrounding primary α phase, and while tension-compression strains could be reduced through simple heat treatment, these strains originating from phase dilation remained concentrated within the martensite after long cycle heat treatment. This is important as locally the microstructure was processed with identically rapid cooling rates, but the phase-localized strains form and stabilize differently than thermal tension-compression asymmetries which can be more easily reduced. This suggests that within the context of multiphase alloys and L-PBF, phase dilation or phase mismatch strains contribute to residual strains alongside thermally driven tension compression asymmetries through a different mechanism which we quantify and must be accounted for in both L-PBF alloy/process design.

2. Experimental Methods and Theory

2.1) Sample Manufacturing, Heat Treatment, and Preparation

A total of 12 spinal cage implants were manufactured on standard commercial Trumpf TruPrint 1000 with the Trumpf recommended 20-um parameter set found in the supplementary Table S.1. The cages were built raised above the built plate on supports oriented as shown in **Figure 1**, with a 51° layer-rotational hatch offset, and no build plate preheating. Real implant geometries were used rather than test coupons to more accurately capture the thermal processing environment and microstructures found in as-built orthopedic implants. Grade 23 extra low interstitial (ELI) Ti-6Al-4V powder in accordance with ASTM F136 was sourced from Trumpf for their manufacture. Parts were cleaned of excess and unsintered powder using pressurized air and sonication in methanol. **Figure 1** shows a digital representation of the spinal cages as processed on the build plate and the support structures utilized. Two separate heat treatment cycles were selected, one above the β transus at 1100°C and one below at 650°C to study solutionizing and strain relief cycles respectively. A Thermo Scientific Lindberg/Blue M tube furnace with fused silica tubes was utilized for all heat treatments. The samples were inserted into the tube and purged with argon, while an argon atmosphere was maintained at a flow rate of .5L/min throughout each run to prevent the effects of oxidation. **Figure 2** shows the time versus temperature plots for each heat treatment cycle utilized in this study. The furnace cooling rate was set using the inbuilt temperature controller and verified by measuring the temperature decrease with the inbuilt thermocouple. The water cooling rate and air cooling rate was estimated to be 650 °C/s and 20 ° C/s respectively, according to *H. Galarraga et al.* [44]

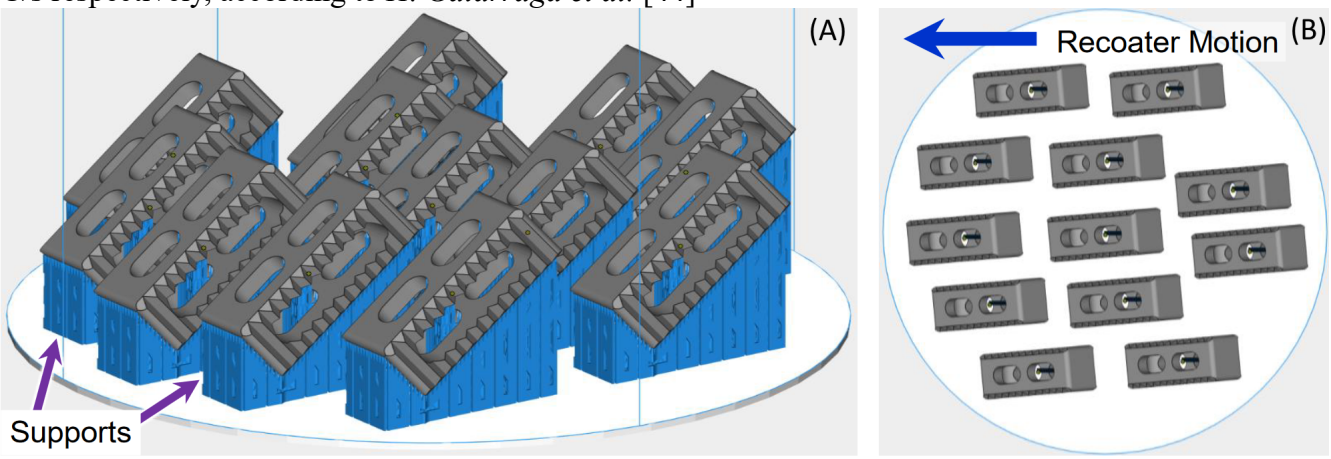

Figure 1: Digital view of the spinal cages as arranged on the build plate from (A) an orthogonal view and (B) a top-plane view highlighting the powder recoating direction.

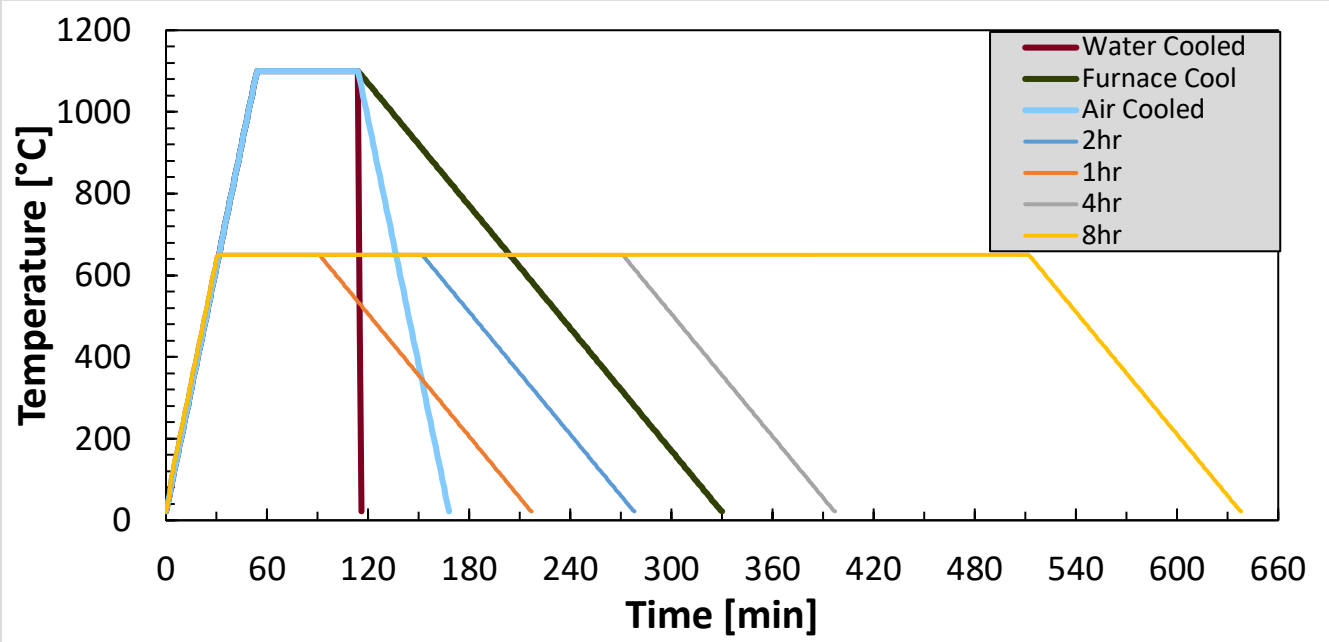

Figure 2: Various heat treatment cycles utilized in sample processing.

Following heat treatment, samples were mounted in cold setting epoxy to image the surface shown in **Figure 3**, not cross sectioned as to retain the as-built strain state, and polished with successively finer grit silicon carbide paper prior to using 6 µm, 3 µm, and 1 µm diamond suspension. Finally, the mounted samples underwent a final polishing step utilizing a 70/30 wt% mixture of .03 µm non-crystalizing colloidal silica and hydrogen peroxide. Samples were then sonicated for 30 minutes and dried prior to performing HR-EBSD. An FEI XL30 ESEM with attached EDAX OIM camera was used to examine the phase distribution and microstructure/orientation of the sample, imaging the top surface of each cage for every sample. The larger area scans shown in **Figure 3** utilized an EBSD step size of 700 nm, the data represented in **Figures 4 and 5** utilize a step size of 150 nm, and lastly the datasets represented in **Figure 7** utilize a step size of 200 nm. GND maps were generated using the built-in function of EDAX's OIM Analysis version 8 software package while inverse pole figure (IPF) orientation maps were generated using the MTEX MATLAB toolbox. [57]–[59]

2.2) HR-EBSD Strain Cross Correlation and Micromechanical Modeling

The Kikuchi pattern cross-correlation analysis for residual strain quantification was calculated with the open-source software package OpenXY [60], with a similar methodology previously described by Small *et. al.* demonstrating that this cross-correlation method could describe the link between dislocation structures and microscale elastic strain in IN625 [61], as well as quantifying the levels of residual strains in IN625 processed by three different AM solidification processes. [16] This process of cross-correlation calculates the rotational shifts between a reference electron back-scattered pattern (EBSP) within each grain and every EBSP within that grain, with a grain being defined by a misorientation tolerance of 5°. OpenXY divides each EBSP into multiple regions of interest (ROI) which contain the Kikuchi lines or their intersections, and by calculating the relative shifts of these features between the reference and test EBSP, the elastic distortion gradient between the grain mean orientation and each point within the grain can be derived from EBSP cross-correlation. The elastic distortion tensor, $\beta=F-I$, produced via measurement of these shifts consists of the deformation gradient tensor, $F=R*U$, and the identity matrix I. The gradient tensor F contains both a rotational component (R) and a strain component (U), where strain is given by $U=I+\varepsilon$, and ε being the elastic strain tensor

itself. Thus, grain relative strain can be determined by measuring the rotational shifts between two EBSPs.

Mesoscopic micromechanical modeling was conducted by taking into account the different elastic moduli of the different phases in solidified Ti-6Al-4V and associated α/β (or α'/β) transformation strains, allowing a comparison of the simulated 3D microscopic strain response to the experimental strain analysis based on 2D information from HR-EBSD. This was done independently of all HR-EBSD measurements, i.e. the model is generated from first principals and not fit from orientation data or experimental results. First, digital representations of 3D phase microstructures of Ti-6Al-4V were generated using phase-field simulations [62] to account for experimentally characterized microstructural features. Note that we focus more on the systematically controlled features to isolate the key physical factors that determine the microscopic strain distribution, rather than accurate prediction of the phase microstructures corresponding to the applied processing/heat treatment conditions. The model considers multiple sources of micro- and mesoscale strains within a microstructure, including phase and thermal strain effects. The phase-dependent elastic moduli [63] were then assigned to corresponding phases within the position-dependent elastic modulus model for the simulated microstructures. The lattice mismatches between α, α', and β phases were considered through the corresponding transformation strains derived based on the associated orientation relationship and lattice parameters. To compute the microstructure-level local strain [64], [65] within the given phase microstructure, the mechanical equilibrium equation was numerically solved using the Fourier-spectral iterative-perturbation method. [65], [66] Further details of the model were discussed in the previous work. [67], [68]

3. Results

3.1) Effect of Residual Strain Relieving Heat Treatment

Strain relief was accomplished by long cycle heat treatments below the recrystallization temperature, which allows for retention of the α phase while allowing for recovery of thermal strains and dislocation annihilation. **Figure 3** shows the imaged surface alongside IPF micrographs for the as-built sample and the sample with the longest heat treatment cycle, highlighting that the higher spatial resolution scans shown in **Figure 4 and 5** are representative of the broader-scale microstructures and that the microstructural morphology is homogeneous within the context of this experiment. **Figure 3** shows that the initial microstructure is dual phase α+α', featuring primary α in both circular and lath morphology with fine needles of martensitic α' distributed between them and no appreciable amounts of β phase detected. After 8 hours of heat treatment, lath coarsening and a reduction in α' is observed which is more clearly seen in the smaller field, finer spatial resolution, micrographs shown in **Figure 5**. **Figure 4** shows the initial microstructure, strain, and GND density distribution of the as-built sample focusing on a smaller scale with higher spatial resolution to highlight the interaction region between phases. Martensitic α' can be observed in **Figure 4** as small orthogonally oriented platelets 'pinned' between elongated and parallel primary α, and in some cases would be too fine to be detected by the larger step-size utilized in **Figure 3**. This morphology is largely maintained throughout heat treatment, with no β phase transformation observed. The effect of the 650°C heat treatment cycle over time is further illustrated by the EBSD results combined in **Figure 5** with the effects on strain relaxation and GND density evident as a function of anneal time. These primary α grains show lower GND density and effective strain values relative to the martensite across all heat treatment times.

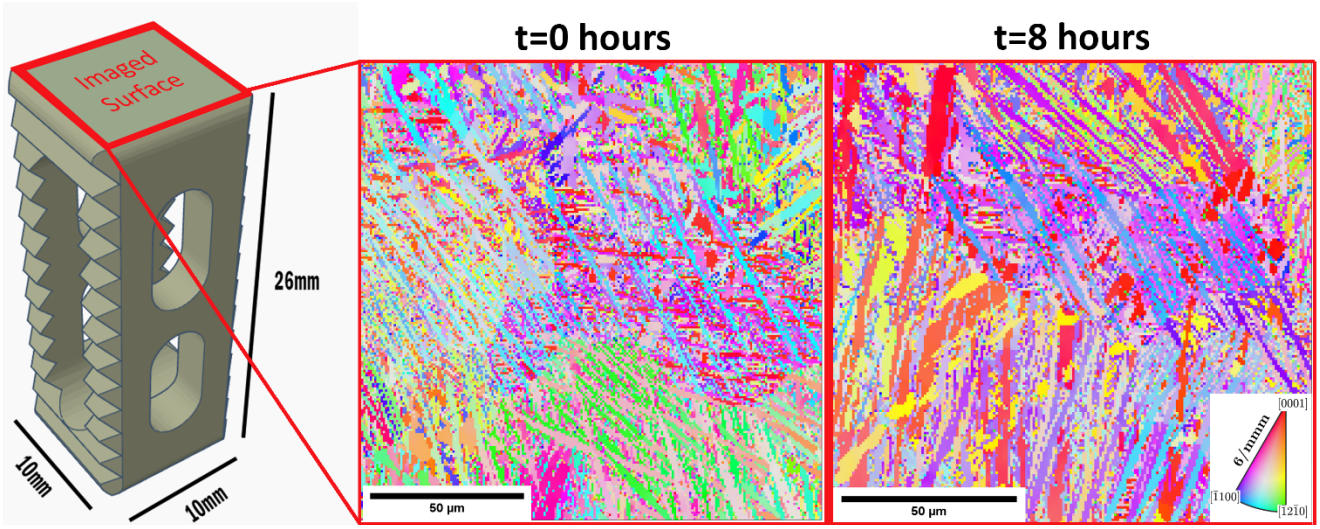

Figure 3: A model spinal cage highlighting the surface from which micrographs were obtained for all samples, and the representative micrographs produced from the as-built sample and the t=8 hours sample.

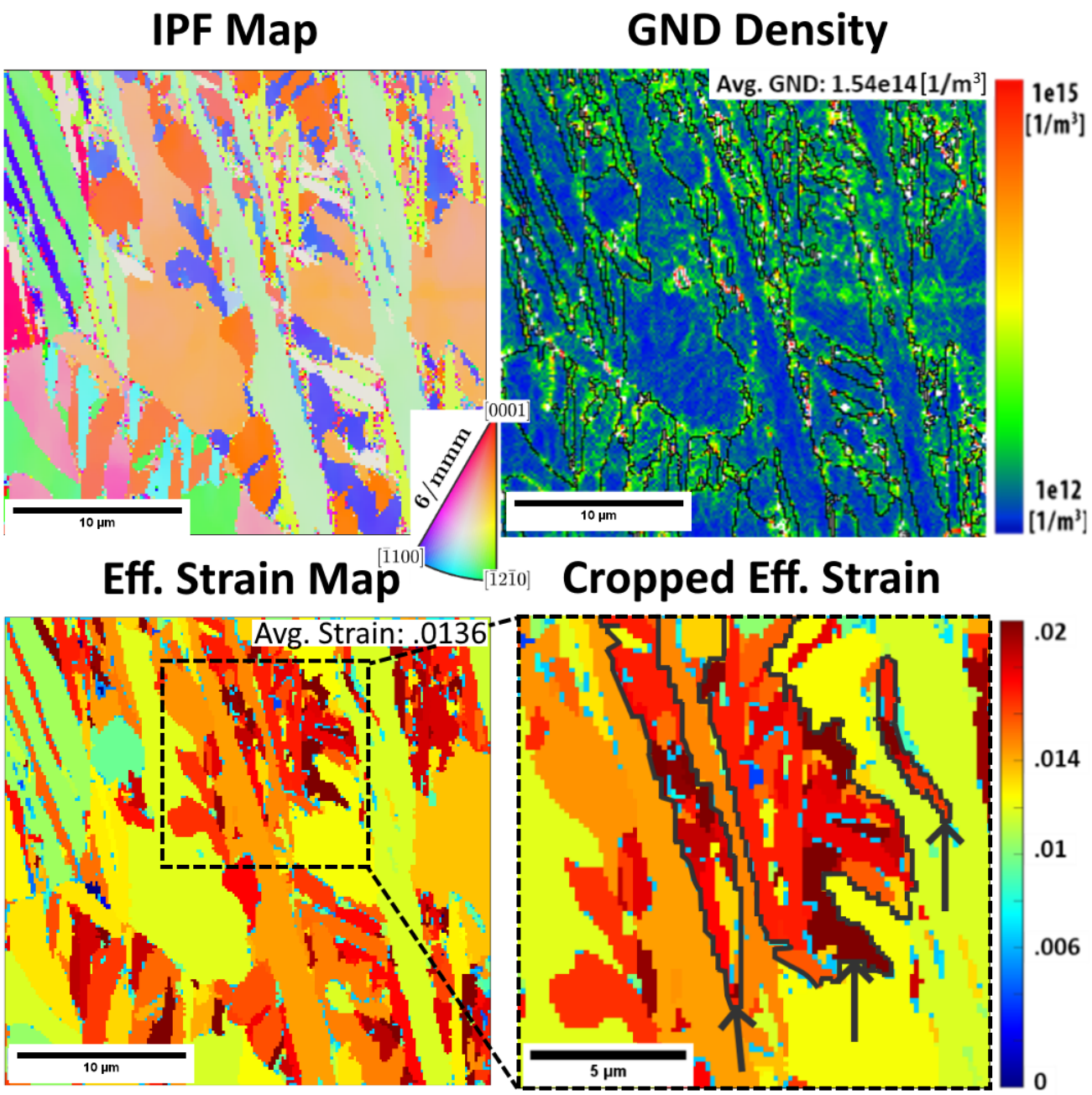

Figure 4: The initial Ti-6Al-4V microstructure as produced by L-PBF, with GND density and strain maps shown and cropped to highlight the strain concentration within the martensite regions highlighted with arrows.

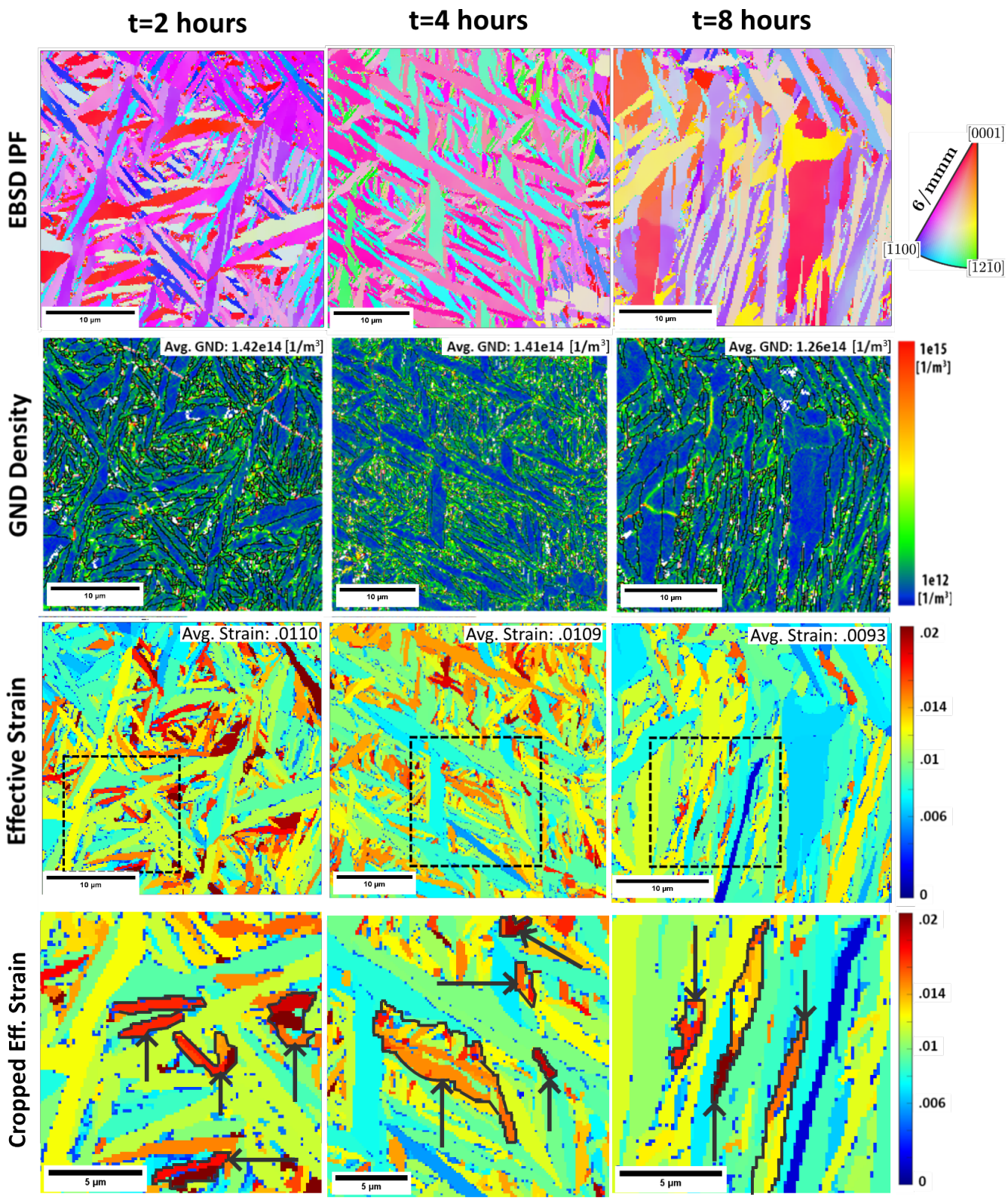

Figure 5: The effect of the 650°C strain relieving anneal cycle as a function of time on microstructure, GND density distribution, and retained strain. Average effective strain and average GND density are given above their respective images. Orientation and strain are shown visualized as a grain average to distinguish fine features. The fine black boxes in the 'Effective Strain' row indicate the regions cropped for the selected areas below, with examples of strain concentration in α' highlighted with black outlines and arrow callouts.

Figure 5 examines how local strain and dislocation density are distributed as a function of microstructure morphology as a function of annealing time. In all samples, the α phase stored less strain and dislocations than the martensitic α' phases surrounding them. High strain fields are evident in retained α', primarily visible pinned between α phase as outlined in the figure, with lower strain observed within the surrounding α grains. The elevated dislocation density distribution within these regions would also suggest these martensite rich regions are more highly strained, showing clusters of higher GND density and thus greater plastic deformation within the martensitic regions. This is cropped for effect in **Figure 5** to highlight this strain concentration occurring within α' phase. This segregation of dislocation density and strains to the martensitic regions is most clear at t=0 and t=4 hours. After 8 hours of heat treatment, although strain has been reduced, GND and strain concentrations are at their highest at α and α' interfacial regions and within α' grains. There is a qualitative reduction in α' phase fraction with increasing heat treatment time, **Figure 5** indicating that there is less observed α' after t=8 hours of heat treatment which accompanies this overall reduction in strain.

The statistical distributions of effective local strain shown in the experimental microstructures in **Figures 4 and 5** are compared to the computationally simulated components of a simulated α+α' microstructure in **Figure 6**. As the annealing time increases, two main features are observed. First, the maximum peak position moves towards to the lower strain values. Second, the breadth of the peak becomes narrower (*i.e.*, peak sharpening). In order to capture the physical origin of these shifting effects within the statistical strain distributions, we performed a parametric micromechanical modeling study with varying phase fractions of α+α' with the values described in **Table 1**. We employed a generated 3D digital microstructure with ~96.4% of (α+α') phases and marginal β phase to capture the L-PBF microstructure observed experimentally. We systematically varied three microstructural and mechanical parameters within the modeling framework to emulate how experimental microstructures would change over time with heat treatment: 1) decreasing volume fraction of the α' phase ($f^{\alpha'}$) to capture martensite decomposition; 2) dilatational lattice strain of the metastable α' phase due to oversaturated alloying components (ε^c); and 3) overall macroscopic strain applied to the microstructure (E^{res}) from longer-ranged thermally induced residual strain. These parameters are shown in **Table 1,** and their effects on the overall strain distributions in **Figure 6(a-c).** Note that, within the model, the α and α' phases are distinguished by ε^c. We then computed the local von Mises strain (ε_{vM}), defined as $(2/3)\sqrt{3(\varepsilon_{11}^2+\varepsilon_{22}^2+\varepsilon_{33}^2)/2+3(\varepsilon_{12}^2+\varepsilon_{23}^2+\varepsilon_{31}^2)/4}$, to obtain the statistical distributions as shown in **Figures 6(a-c)**.

Our modeling shows that the strain distribution is sensitive to all of those factors, and in order for the microstructure model to accurately capture experimental results. In particular, **Figures 6(a,b)** indicate that the strain peak position is mainly controlled by $f^{\alpha'}$ and ε^c. Specifically, the maximum peak position moves towards to the lower value as $f^{\alpha'}$ decreases (see **Figure 6(a)**) or ε^c decreases (see **Figure 6(b)**). These correspond to the effects of α' decomposition and redistribution of the alloying elements with increased heat treatment time, respectively. It should be noted that the breadth of the peak is not sensitive to $f^{\alpha'}$ and ε^c. Rather, the breadth of the peak is largely controlled by the macroscopic strain applied to the entire microstructure as shown in **Figure 6(c)**. This means that the peak can be sharpened, and strain distribution narrowed, as the macroscopic thermal strains are relaxed. More importantly, we indicate that variation of a single parameter cannot reproduce the experimentally observed behavior (**Figure 6(d)**) of the strain statistics without accounting for both microscale phase contributions *and* thermally driven macroscopic strains. Rather, the main features of the strain statistics behavior in terms of the peak position and the breadth can be captured only when two or more microstructural and mechanical parameters ($f^{\alpha'}$, ε^c, E^{res}) are convoluted. Therefore, we may

reproduce the experimentally observed behavior of the asymmetric strain distributions in **Figure 6(d)** by simultaneously accounting for phase fraction and dilatational strains in addition to macroscopic thermal ones. For example, the computed strain distributions with the combined factors will reproduce in simulation the experimentally observed strain distribution behavior seen changing with the annealing time (see **Figure 6(e)**). We emphasize that the reproduced features by 3D simulations rationalize the validity of our experimental analysis based on 2D microstructural information from HR-EBSD, showing that the microscale phase contributions to the overall strain distribution are distinct from thermally driven strains and are relaxed via dissolution of the martensite.

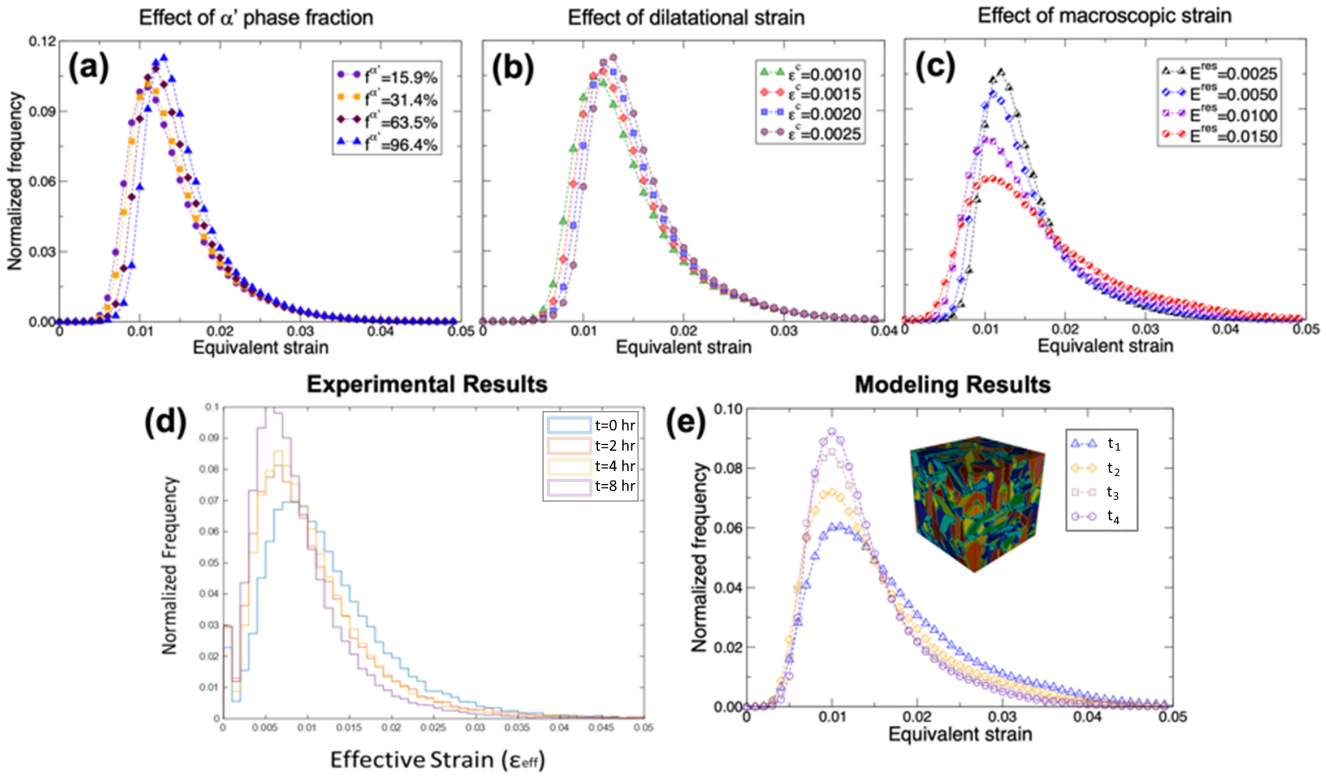

Figure 6: Statistical distributions of von Mises strain in Ti-6Al-4V microstructures: (a) computed strain distributions for different α' phase fractions, (b) computed strain distributions for different dilatational strains, (c) computed strain distributions for different macroscopic strains, (d) variation of the experimentally characterized strain distribution with annealing time in comparison to (e) the simulated strain relaxation combining the three effects in (a)-(c) for the modeled microstructures.

Table 1: Microstructural and mechanical parameters for the micromechanical modeling of local strain for different annealing times.

Annealing time	f^{α}	$f^{\alpha'}$	E^{res}	ε^{c}
t_1	0%	96.4%	0.0150	0.0025
t_2	32.9%	63.5%	0.0125	0.0020
t_3	65.0%	31.4%	0.0075	0.0015

t_4	80.5%	15.9%	0.0050	0.0010

3.2) Effect of β annealing and cooling on residual strain and microstructure

Often an increase in ductility and toughness is afforded by dual-phase (α+β) Ti-6Al-4V, and the generation of a more equiaxed and isotropic microstructure is desirable in many applications. To achieve this dual-phase microstructure, a solutionizing heat treatment above the β transus of ~1000°C is required. **Figure 7** shows the experimentally observed microstructural effect of heating above the β transus and cooling under three commonly used conditions. Furnace cooling (5 °C/s) resulted in the largest fields of retained β, located between large α platelets. Meanwhile, water cooling (~ 650 °C/s) resulted in a fine acicular α' dominated microstructure with a small amount of transformed β, mostly retained along prior grain boundaries edges. No primary α was observed in the case of water cooling. Air cooling (~ 20 °C/s) resulted in a platelet and primary α dominated microstructure, with a small volume of fine α' near regions of primary α and a negligible amount of β retention. These changes in microstructure and phase content would indicate that there was little to no retention of the original, as-manufactured, microstructure.

The slow cooling rate present in the furnace-cooling condition resulted in a very low residual strain distribution, lower strain than observed in the longest strain-relieving cycles shown in **Figure 5**, with strain maxima being focused within retained β phase and between α-β interfaces. The water-cooling condition resulted in higher residual strain than the as-manufactured condition in **Figure 5**. The strain distribution of the water-cooled sample mimics that of the as-built and strain relieved samples, with high strain being observed primarily among the smaller α' laths while the larger grains show a lower strain distribution. The intermediate case of air-cooling, which produced an α dominated microstructure, also resulted in a very low overall residual strain distribution (relative to the as-built condition) with pockets of higher residual strain observed along the interfaces between α and α' grains.

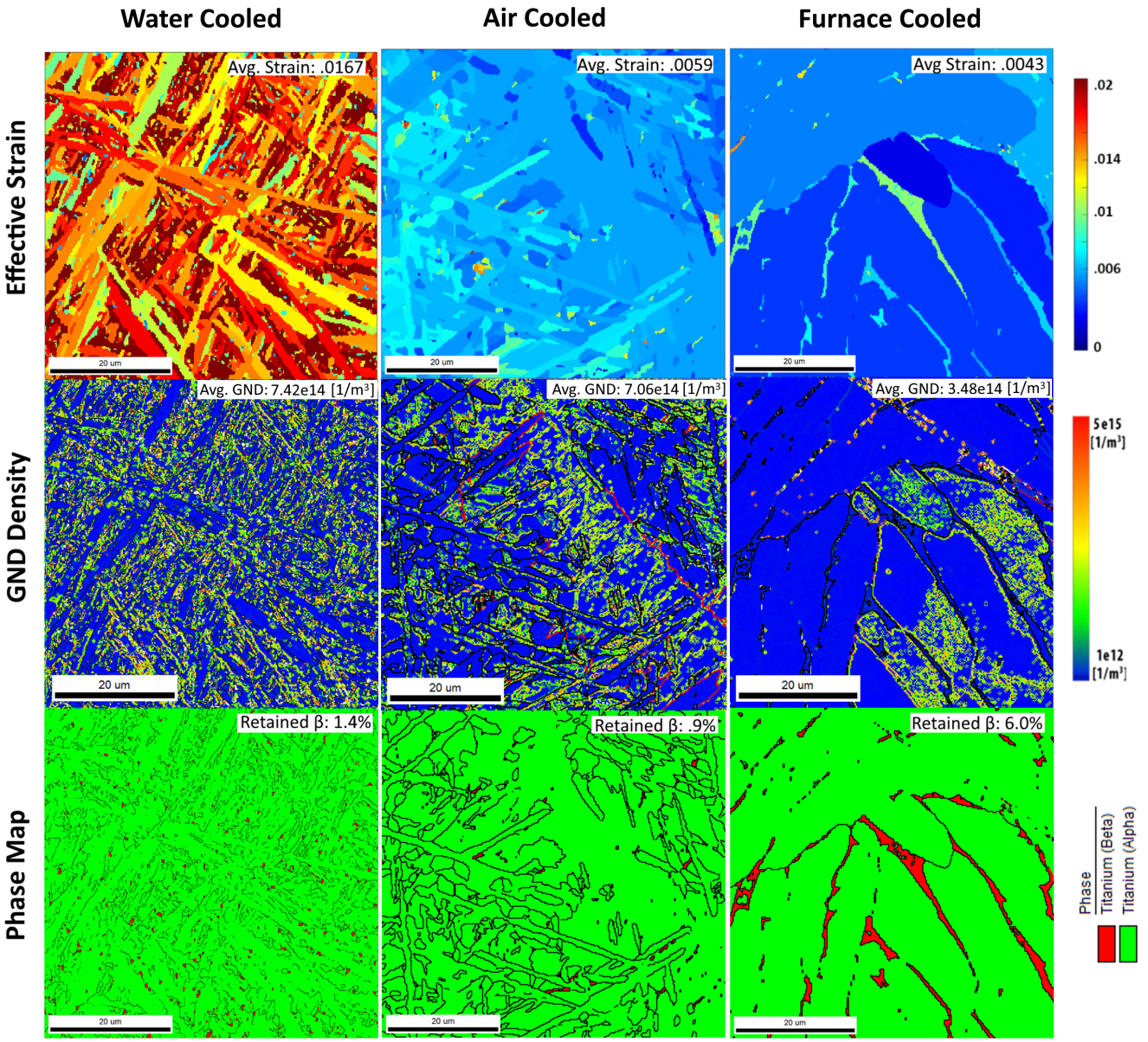

Figure 7: Experimentally characterized strain and phase maps of Ti-6Al-4V after β annealing, studied under three different cooling conditions.

We also examined the spatial profiles of local strains and statistical strain distributions using the micromechanical modeling approach. For comparison, we employed 3 cases of digital representations of phase microstructures: 1) (α+β) two-phase microstructure for the furnace cooling case; 2) (α+α') phase microstructure for the air-cooling case; and 3) α' phase microstructure for the water-cooling case. We assumed $\varepsilon^c = 0.0025$ for the α' phase. We also assumed $E^{res} = 0.00$ for the furnace-cooling case, $E^{res} = 0.01$ for the air-cooling case, and $E^{res} = 0.02$ for the water-cooling case. **Figures 8(a) and 8(c)** show the simulated 3D strain maps of the local von Mises strain and their collected statistical distributions, respectively. The simulated strain maps in **Figure 8(a)** clearly show that slower cooling rate results in lower local strain, which is consistent with the experimental analysis above. In addition, the reproduced strain distributions well capture the major features of the experimentally characterized strain distributions (see **Figure 8(c)** in comparison with **Figure 8(b)**) in terms of the peak positions and the peak breadths for different cooling methods. The (α+β) microstructure for the furnace-cooled case

shows lower strain than the mostly martensitic water-cooled case, meanwhile the air-cooled microstructure containing mostly α and α' phases exhibits a distribution somewhere in the middle. In addition, the simulated strain peaks become broader as the cooling rate increases as observed in the experimental analysis. This also indicates that the cooling rate simultaneously influences the microstructural and mechanical parameters (*i.e.*, $f^{\alpha'}$, ε^c, E^{res}), resulting in the observed strain distribution behavior.

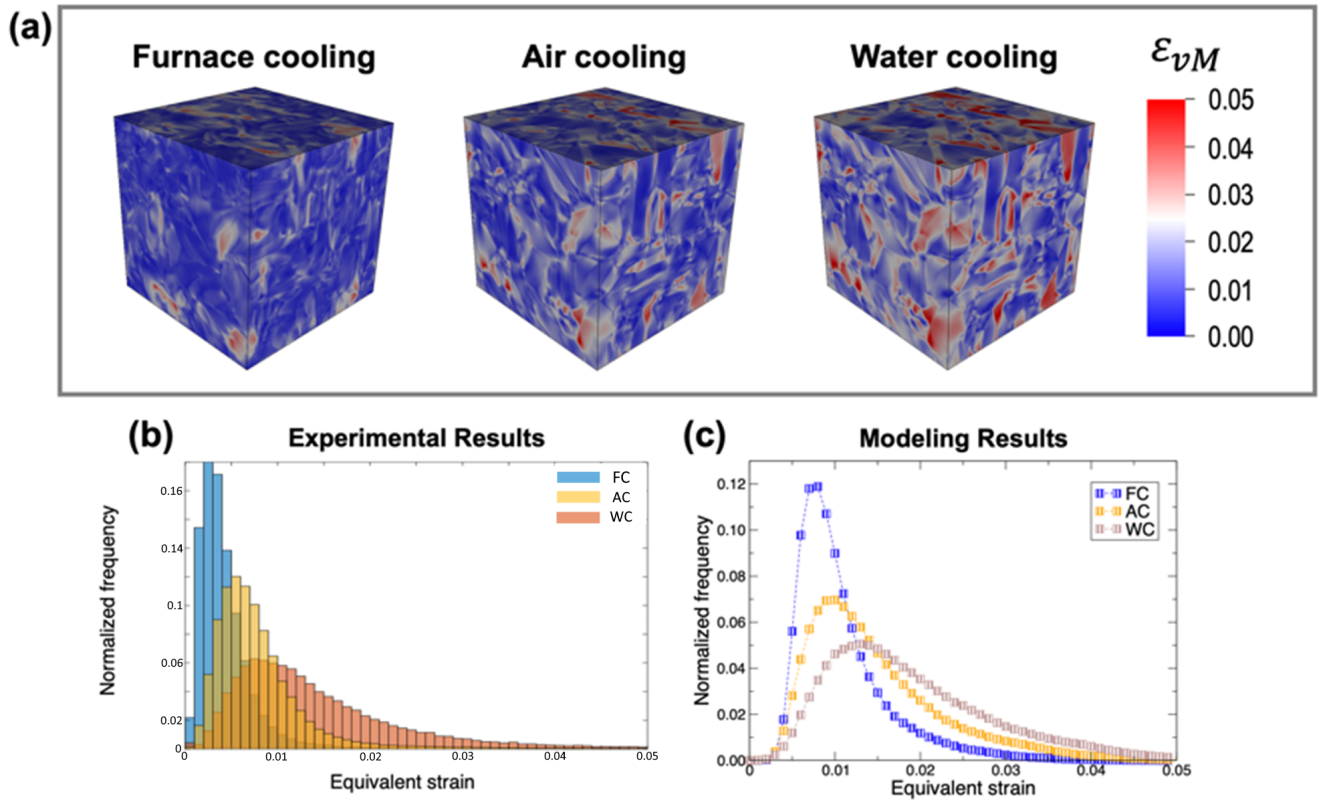

Figure 8: (a) Computed 3D strain maps in digital representations of Ti-6Al-4V microstructures corresponding to the three cooling methods (Furnace cooling: $f_v^{\alpha} = 69.8\%$, $f^{\alpha'} = 0\%$; Air cooling: $f_v^{\alpha} = 65.0\%$, $f^{\alpha'} = 31.4\%$; Water cooling: $f_v^{\alpha} = 0\%$, $f^{\alpha'} = 96.4\%$). Statistical distributions of von Mises strain for the three cooling methods from (b) experimental characterizations and (b) micromechanical modeling.

4. Discussion

These results demonstrate the evolution of microscale residual strain as a function of post-processing heat treatment through the lens of microstructure, GND density, and phase morphology in order to deconvolute and model the sources of strains at the microscale from the influence of macroscopic thermal strains. While reporting that average residual strains are relaxed and decrease with heat treatment is not a novel observation, by deconvoluting the different contributing sources of these strains at the microscale we are able to glean new information about how strain generation and relaxation mechanisms evolve and are dependent on the phase morphology. Specifically, we show that martensite retention creates dilatational lattice strains both inter- and intragranularly via a different mechanism than macroscale thermal strains, and in order to accommodate this increased lattice strain and internal curvature, higher GND density is present and retained through long cycle heat treatment as

a strain mediation mechanism. Martensitic grains consistently featured higher strain and GND density and retained this higher density after heat treatment, as the slower process of vanadium diffusion and martensite dissolution limit this dilatational strain relaxation and would require a phase transformation for full relaxation and dislocation annihilation. Yet, in the primary α grains macroscale thermal tension-compression asymmetries are reduced through dislocation annihilation and these internal strains are preferentially relaxed alongside a GND density decrease in the α phase. The specific contributions of microscale strains formed from the diffusionless transformation of β to α' phase within Ti-6Al-4V and its contribution the broader scale residual strain distribution and its retention have been quantified via HR-EBSD and validated by 3D mesoscopic micromechanical modeling. In **Figure 6** we demonstrate that in order to accurately capture the experimentally observed strain distribution in simulated microstructures there are three major contributors to microscale strain: lattice mismatch between phases ($f^{\alpha'}$), dilatational strain within the martensite due to vanadium substitution within the lattice (ε^{c}), and macroscopic thermal stresses (E^{res}). The model reflects the experimental results from the heat treatment study shown in **Figure 4** and **Figure 5**, the as-built sample showed higher average strain across the microstructure from a convolution of both microscale lattice strains and macroscale thermal strains. As heat treatment continues, macroscale thermal strains are relaxed leading to a decrease in average strain while incomplete martensite dissolution allowed strain to remain concentrated in retained α' due to lattice mismatch and dilation, and this is reflected in the strain distributions in **Figure 6(d).** Consequently, this confirms that thermal strains are still retained in the diffraction volume on the polished surface, as they are measurably reduced with heat treatment and simulated strained volumes capture the same strain distributions. Higher dislocation density in the martensite in both as-built and heat treated conditions confirms and trends with previous research, and further validates our data. [40] The strain at the interfaces between primary α and martensitic α', and higher strain within α', should be highlighted as it confirms the phenomena of dilatational strain from increased V content in the α' grains. [41] Although we are unable to precisely quantify the phase fraction of α' from the micrographs alone, utilizing the comparison to a simulated microstructure in **Figure 6** supports and confirms this strain localization and retention in the α' phase. The microstructures modeled and strains calculated in **Figure 6** closely trend with the experimental results in **Figure 5**, with overall residual strain decreasing as macroscopic thermal strains are reduced while the dilatory strain contribution from the α'phase is only reduced through a reduction in the phase fraction of α' and conversion to α. The simulations are only able to accurately reflect experimental microscale strain once this dilatory, phase generated, strain from the martensite is factored in.

The residual strain retention and phase stabilization shown here in Ti-6Al-4V are similar to how martensite in steel produces a lattice distortive strain (Bain strain), however it should be noted that in titanium this is due to vanadium substitution rather than carbon interstitials in steel. [37] As studied in steel, the lattice strain serves to reduce the driving force of further martensitic transformation and stabilizes the nascent martensite phase. This interplay of strain and phase formation has further implications in multi-phase alloy systems. The topology of martensite and austenite phases is controlled via residual strain energy as the strain energy released by the martensite serves as the driving force for transforming to austenite. [69] This has impact on the bulk performance of these materials as shown in laser-processed steels, previous studies indicating that microscale control of dislocation density as a function of martensite expression would result in reduced fatigue life. [70] We show that a similar codependency between strain energy and the chemical driving force of phase transformation is observed in L-PBF Ti-6Al-4V as enabled by the rapid solidification during L-PBF. The vanadium solute is in higher concentrations in the metastable α' phase than the stable α phase, retaining the chemical composition of prior β grains due to the diffusionless transformation, which leads to a greater lattice straining effect in the martensite. [49], [71] The lattice straining effect caused by the

oversaturated alloying elements in the metastable phase is also evidenced by our controlled micromechanical simulations by varying the dilatational strain (see **Figure 6(b)**) and the elevated strain seen within the martensite in **Figure 4 and 5**. We indicate that both the decomposition of the α' phase incorporating the lattice strain (phase-mismatch strain relaxation with decreasing α' phase fraction, **Figure 6(a)**) and the redistribution of the alloying elements (the strain relaxation with the decreasing dilatational strain, **Figure 6(b)**) serve as mechanisms to reduce the internal microscopic strain. This highlights the interdependency of α/α'phase stability and morphology as a function of retained strain, and the ability to control the residual strain distribution in L-PBF AM via localized microstructure tuning through laser process parameters. [72] In addition, our analysis verifies that the L-PBF process does not just introduce strains by thermal gradients alone, but that these rapid cooling rates promote phase dependent lattice strains which influence phase stability and the overall strain distribution.

It is important to note that the relaxing behavior of these microscopic strains associated with α' phase decomposition and solute redistribution occurs in concert with relaxation of the macroscopic strains (*e.g.*, thermal gradient-induced strain). Again, this is because of the balance of strain stabilizing one phase, while the relaxation of strains through vanadium diffusion enables transformation of the metastable α' to the α phase. This is evidenced by the excellent agreement between experimental (**Figure 6(d)**) and modeling (**Figure 6(e)**) results in terms of the peak breadth variation (*i.e.*, sharpening with the annealing time). Therefore, we conclude that the dynamics of microscale strain relaxation in L-PBF Ti-6Al-4V undergoing heat treatment is determined by the convolution of solute redistribution, phase decomposition, and thermal gradient-induced strain relaxation and cannot be easily explained by one mechanism. Accordingly, this indicates that overall residual strain within the context of L-PBF AM incorporates not only strain buildup of macroscopic thermal tension/compression fields, but also shows a codependence on lattice strain arising from metastable phase morphology, solute supersaturation, and their spatial configurations. [21]

Strain localization within phases and convolution of different strain mechanisms is also mirrored in samples undergoing solutionizing from above the β transus, in **Figures 8(b)** and **(c)**, indicating that the microstructure-level strain is not simply determined by the L-PBF process-induced macroscale thermal strains, but is inherent to microstructure evolution and thermal processing. As shown in **Figures 7** and **8,** the solutionizing heat treatments lead to decomposition of the α' phase, resulting in a net reduction of residual strain. The furnace and air-cooled microstructure shown in **Figure 7** indicate that lower residual stresses are achieved as a function of phase morphology in addition to cooling rates, achieving lower stresses than the (α+α') microstructures in **Figures 4 or 5** even after long cycle heat treatment where thermal strains would have been reduced through recovery. This is verified by the simulated microstructures in **Figure 8**, which also demonstrate higher strain in the martensite dominated microstructure than in the (α+β) microstructure. The water-cooled and air-cooled conditions feature a similar microstructure to that observed in the as-built L-PBF sample, with different distributions of α and α'. Both these samples show phase localized strain, showing higher strain concentration in the small α' needles than primary α where present. When performing solutionizing heat treatment with a slow furnace cooling to create a dual-phase (α+β) microstructure, the α phase is less strained relative to the β phase, which retains a majority of the strain and GND concentration present in the microstructure. The partitioning of strain between the α and β phases has been recently validated via *in-situ* experiments, with strain localization bands occurring at the early stages of plastic deformation. [73] Building on those results, we show that the partitioning of strain is tied to the phase distribution of the two micromechanically distinct phases and can occur in unstrained, heat treated, samples in addition to plastically deformed samples. In addition, in the phase growth process of slow furnace annealing,

growing α grains could impinge on retained β, plastically deforming them and generating higher GND densities within these β phase regions shown in **Figure 7**.

It should be cautioned here that our modeling does not take into account exactly the same microstructures as the experimental counterparts in terms of content, orientation, and spatial configuration even though key physical features and equivalencies are accounted for within the micromechanical modeling context. The model was developed independently, without fitting or HR-EBSD strain data input to the model, and the strain distribution in our micromechanical model can still accurately capture experimental microstructures by accounting for the three critical strain inputs we studied. The general framework of a combined experiment-modeling approach that links phase content, the associated microstructure, macroscale thermal strains, and their effects on local strains provides a means to better understand how residual strain forms and is relaxed across scale in rapidly cooled microstructures and how strains can be controlled through microstructural engineering via L-PBF process control.

5. Conclusion

We produced L-PBF Ti-6Al-4V with a martensite dominated microstructure, which was post-processed by various heat treatment cycles, in order to understand how phase driven lattice-dilatational strains at the microscale and macroscale thermal strains are convoluted and contribute to residual strain in L-PBF components. A combined experiment-modeling approach was applied to analyze the retention and generation of microscale strains as a response to the different phase morphologies and microstructures that result from heat treatment and different cooling rates. The relationship between processing conditions, microstructure, and residual strain demonstrated by this approach indicates that the magnitude of residual strain is determined by the phase fraction and distribution of mismatched phases at the grain and subgrain scale, while macroscale thermal strains drive the overall width of the strain distribution and account for the higher strain values within that distribution. This emphasizes that phase-induced strains at the microscale contribute to the overall residual strain of Ti-6Al-4V fabricated via L-PBF through a different mechanism than the part-spanning thermally driven macroscale residual strains in L-PBF AM.

While it is a rapid cooling rate which generates the martensite through diffusionless transformation, the origin of this strain is from local lattice expansion within the α’ phase and lattice mismatch between the surrounding α phase, not due to thermally driven tension-compression asymmetries. This is confirmed via micromechanical modeling, which shows that only by accounting for both microscale and macroscale strain contributions can an experimentally accurate strain distribution be reached. Microscale strain serves to stabilize the α’ phase, and influences further phase transformation because of this strain-phase codependency. We also verified that the internal lattice strain and high dislocation content present in α’ Ti-6Al-4V persists even after long cycle strain relieving heat treatment. This indicates that full relaxation of the residual strain is only possible through decomposition of the α’ phase and the redistribution of alloying elements (*e.g.*, vanadium) which cause the lattice dilation. Within the greater context of L-PBF AM, this suggests that tuning residual strain through microstructure could be an effective engineering strategy for controlling site-specific mechanical properties at the microscale.

Acknowledgments

The authors acknowledge helpful discussions with Dr. Saad A. Khairallah (LLNL). The work performed at JHU was funded in part by the U.S. Department of Energy by Lawrence Livermore

National Laboratory (LLNL) under Contract B646330 and in part by the Office of Naval Research under contract N00014-20-1-2788. The simulation work performed by LLNL was funded by the Laboratory Directed Research and Development program at LLNL under the project tracking code 18-SI-003.

Data Availability

The raw data (EBSD patterns) required to reproduce these findings cannot be shared at this time due to technical or time limitations. The processed data required to reproduce these findings are available to download from the following DOI: 10.17632/zzdjysc98c.2 [74]

References

[1] J. P. Kruth, "Material Incress Manufacturing by Rapid Prototyping Techniques," *CIRP Ann. - Manuf. Technol.*, vol. 40, no. 2, pp. 603–614, 1991, doi: 10.1016/S0007-8506(07)61136-6.

[2] R. Huang *et al.*, "Energy and emissions saving potential of additive manufacturing: the case of lightweight aircraft components," *J. Clean. Prod.*, vol. 135, pp. 1559–1570, 2016, doi: 10.1016/j.jclepro.2015.04.109.

[3] L. Parry, I. A. Ashcroft, and R. D. Wildman, "Understanding the effect of laser scan strategy on residual stress in selective laser melting through thermo-mechanical simulation," *Addit. Manuf.*, vol. 12, pp. 1–15, 2016, doi: 10.1016/j.addma.2016.05.014.

[4] R. K. Gupta, V. A. Kumar, C. Mathew, and G. S. Rao, "Strain hardening of Titanium alloy Ti6Al4V sheets with prior heat treatment and cold working," *Mater. Sci. Eng. A*, vol. 662, pp. 537–550, 2016, doi: 10.1016/j.msea.2016.03.094.

[5] P. Bocchetta, L. Chen, J. Dias, C. Tardelli, F. Almeraya-calder, and P. Leo, "Passive Layers and Corrosion Resistance of Biomedical Ti-6Al-4V and β -Ti Alloys," 2021.

[6] F. Calignano, M. Galati, L. Iuliano, and P. Minetola, "Design of Additively Manufactured Structures for Biomedical Applications : A Review of the Additive Manufacturing Processes Applied to the Biomedical Sector," vol. 2019, 2019.

[7] M. Sharma and M. Soni, "Materials Today : Proceedings Direct metal laser sintering of TI6Al4V alloy for patient-specific temporo mandibular joint prosthesis and implant," *Mater. Today Proc.*, vol. 38, pp. 333–339, 2021, doi: 10.1016/j.matpr.2020.07.417.

[8] C. Oldani and A. Dominguez, "Titanium as a Biomaterial for Implants," *Recent Adv. Arthroplast.*, 2012, doi: 10.5772/27413.

[9] R. Van Noort, "Titanium: The implant material of today," *J. Mater. Sci.*, vol. 22, no. 11, pp. 3801–3811, 1987, doi: 10.1007/BF01133326.

[10] A. M. Khorasani, M. Goldberg, E. H. Doeven, and G. Littlefair, "Titanium in biomedical applications—properties and fabrication: A review," *J. Biomater. Tissue Eng.*, vol. 5, no. 8, pp. 593–619, 2015, doi: 10.1166/jbt.2015.1361.

[11] B. Vandenbroucke and J. P. Kruth, "Selective laser melting of biocompatible metals for rapid manufacturing of medical parts," *Rapid Prototyp. J.*, vol. 13, no. 4, pp. 196–203, 2007, doi: 10.1108/13552540710776142.

[12] Y. He, D. Burkhalter, D. Durocher, and J. M. Gilbert, "Solid-Lattice Hip Prosthesis Design: Applying Topology and Lattice Optimization to Reduce Stress Shielding From Hip Implants," pp. 1–5, 2018, doi: 10.1115/dmd2018-6804.

[13] S. Arabnejad, B. Johnston, M. Tanzer, and D. Pasini, "Fully porous 3D printed titanium femoral stem to reduce stress-shielding following total hip arthroplasty," *J. Orthop. Res.*, vol. 35, no. 8, pp. 1774–1783, 2017, doi: 10.1002/jor.23445.

[14] S. Maietta, A. Gloria, G. Improta, M. Richetta, R. De Santis, and M. Martorelli, "A further

analysis on Ti6Al4V lattice structures manufactured by selective laser melting," *J. Healthc. Eng.*, vol. 2019, 2019, doi: 10.1155/2019/3212594.
[15] A. Jiménez, P. Bidare, H. Hassanin, F. Tarlochan, S. Dimov, and K. Essa, "Powder-based laser hybrid additive manufacturing of metals : a review," pp. 63–96, 2021.
[16] K. A. Small and M. L. Taheri, "Role of Processing in Microstructural Evolution in Inconel 625: A Comparison of Three Additive Manufacturing Techniques," *Metall. Mater. Trans. A Phys. Metall. Mater. Sci.*, vol. 52, no. 7, pp. 2811–2820, 2021, doi: 10.1007/s11661-021-06273-x.
[17] S. Liu and Y. C. Shin, "Additive manufacturing of Ti6Al4V alloy: A review," *Mater. Des.*, vol. 164, p. 107552, 2019, doi: 10.1016/j.matdes.2018.107552.
[18] T. Vilaro, C. Colin, J. D. Bartout, L. Nazé, and M. Sennour, "Microstructural and mechanical approaches of the selective laser melting process applied to a nickel-base superalloy," *Mater. Sci. Eng. A*, vol. 534, pp. 446–451, 2012, doi: 10.1016/j.msea.2011.11.092.
[19] L. Zheng, Y. Liu, S. Sun, and H. Zhang, "Selective laser melting of Al-8.5Fe-1.3V-1.7Si alloy: Investigation on the resultant microstructure and hardness," *Chinese J. Aeronaut.*, vol. 28, no. 2, pp. 564–569, 2015, doi: 10.1016/j.cja.2015.01.013.
[20] P. Mercelis and J. P. Kruth, "Residual stresses in selective laser sintering and selective laser melting," *Rapid Prototyp. J.*, vol. 12, no. 5, pp. 254–265, 2006, doi: 10.1108/13552540610707013.
[21] Y. Liu, Y. Yang, and D. Wang, "A study on the residual stress during selective laser melting (SLM) of metallic powder," *Int. J. Adv. Manuf. Technol.*, 2016, doi: 10.1007/s00170-016-8466-y.
[22] W. Chen *et al.*, "Microscale residual stresses in additively manufactured stainless steel," *Nat. Commun.*, vol. 10, no. 1, pp. 1–12, 2019, doi: 10.1038/s41467-019-12265-8.
[23] K. A. Small and M. L. Taheri, "Multiscale Characterization of Microstructure and Residual Strain Distribution in Additively Manufactured Inconel 625," *Microsc. Microanal.*, vol. 25, no. S2, pp. 2586–2587, 2019, doi: 10.1017/s1431927619013667.
[24] M. Megahed, H.-W. Mindt, N. N'Dri, H. Duan, and O. Desmaison, "Metal additive-manufacturing process and residual stress modeling," *Integr. Mater. Manuf. Innov.*, 2016, doi: 10.1186/s40192-016-0047-2.
[25] J. P. Oliveira, T. G. Santos, and R. M. Miranda, "Revisiting fundamental welding concepts to improve additive manufacturing: From theory to practice," *Prog. Mater. Sci.*, vol. 107, no. June 2019, p. 100590, 2019, doi: 10.1016/j.pmatsci.2019.100590.
[26] N. C. Levkulich, S. L. Semiatin, J. E. Gockel, J. R. Middendorf, A. T. DeWald, and N. W. Klingbeil, "The effect of process parameters on residual stress evolution and distortion in the laser powder bed fusion of Ti-6Al-4V," *Addit. Manuf.*, vol. 28, no. January, pp. 475–484, 2019, doi: 10.1016/j.addma.2019.05.015.
[27] P. Edwards and M. Ramulu, "Fatigue performance evaluation of selective laser melted Ti-6Al-4V," *Mater. Sci. Eng. A*, vol. 598, pp. 327–337, 2014, doi: 10.1016/j.msea.2014.01.041.
[28] V. Chastand, A. Tezenas, Y. Cadoret, P. Quaegebeur, W. Maia, and E. Charkaluk, "Fatigue characterization of Titanium Ti-6Al-4V samples produced by Additive Manufacturing," *Procedia Struct. Integr.*, vol. 2, pp. 3168–3176, 2016, doi: 10.1016/j.prostr.2016.06.395.
[29] A. Sterling, N. Shamsaei, B. Torries, and S. M. Thompson, "Fatigue Behaviour of Additively Manufactured Ti-6Al-4 v," *Procedia Eng.*, vol. 133, pp. 576–589, 2015, doi: 10.1016/j.proeng.2015.12.632.
[30] D. Banerjee and J. C. Williams, "Perspectives on titanium science and technology," *Acta Mater.*, vol. 61, no. 3, pp. 844–879, 2013, doi: 10.1016/j.actamat.2012.10.043.
[31] L. Thijs, F. Verhaeghe, T. Craeghs, J. Van Humbeeck, and J. P. Kruth, "A study of the microstructural evolution during selective laser melting of Ti-6Al-4V," *Acta Mater.*, vol. 58, no. 9, pp. 3303–3312, 2010, doi: 10.1016/j.actamat.2010.02.004.
[32] P. A. Kobryn and S. L. Semiatin, "The laser additive manufacture of Ti-6Al-4V," *JOM*, vol. 53,

no. 9, pp. 40–42, 2001, doi: 10.1007/s11837-001-0068-x.
[33] A. L. Pilchak, G. A. Sargent, and S. L. Semiatin, “Early Stages of Microstructure and Texture Evolution during Beta Annealing of Ti-6Al-4V,” *Metall. Mater. Trans. A Phys. Metall. Mater. Sci.*, vol. 49, no. 3, pp. 908–919, 2018, doi: 10.1007/s11661-017-4444-8.
[34] J. Sieniawski, W. Ziaja, K. Kubiak, and M. Motyka, *Titanium alloys: advances in properties control*. IntechOpen, 2013.
[35] G. Lutjering and J. C. Williams, *Titanium*. Springer Science & Buisness Media, 2007.
[36] A. M. Beese and B. E. Carroll, “Review of Mechanical Properties of Ti-6Al-4V Made by Laser-Based Additive Manufacturing Using Powder Feedstock,” *JOM*, vol. 68, no. 3, pp. 724–734, 2016, doi: 10.1007/s11837-015-1759-z.
[37] M. Motyka, “Martensite formation and decomposition during traditional and am processing of two-phase titanium alloys—an overview,” *Metals (Basel).*, vol. 11, no. 3, pp. 1–18, 2021, doi: 10.3390/met11030481.
[38] M. Zaiser and E. C. Aifantis, “Geometrically necessary dislocations and strain gradient plasticity - A dislocation dynamics point of view,” *Scr. Mater.*, vol. 48, no. 2, pp. 133–139, 2003, doi: 10.1016/S1359-6462(02)00341-X.
[39] S. Sun, B. L. Adams, and W. E. King, “Observations of lattice curvature near the interface of a deformed aluminium bicrystal,” *Philos. Mag. A Phys. Condens. Matter, Struct. Defects Mech. Prop.*, vol. 80, no. 1, pp. 9–25, 2000, doi: 10.1080/01418610008212038.
[40] S. Cao *et al.*, “Role of martensite decomposition in tensile properties of selective laser melted Ti-6Al-4V,” *J. Alloys Compd.*, vol. 744, pp. 357–363, 2018, doi: 10.1016/j.jallcom.2018.02.111.
[41] E. Sallica-Leva, R. Caram, A. L. Jardini, and J. B. Fogagnolo, “Ductility improvement due to martensite α’ decomposition in porous Ti-6Al-4V parts produced by selective laser melting for orthopedic implants,” *J. Mech. Behav. Biomed. Mater.*, vol. 54, pp. 149–158, 2016, doi: 10.1016/j.jmbbm.2015.09.020.
[42] S. L. Semiatin *et al.*, “Dissolution of the Alpha Phase in Ti-6Al-4V During Isothermal and Continuous Heat Treatment,” *Metall. Mater. Trans. A Phys. Metall. Mater. Sci.*, vol. 50, no. 5, pp. 2356–2370, 2019, doi: 10.1007/s11661-019-05164-6.
[43] S. Leuders *et al.*, “On the mechanical behaviour of titanium alloy TiAl6V4 manufactured by selective laser melting: Fatigue resistance and crack growth performance,” *Int. J. Fatigue*, vol. 48, pp. 300–307, 2013, doi: 10.1016/j.ijfatigue.2012.11.011.
[44] H. Galarraga, R. J. Warren, D. A. Lados, R. R. Dehoff, M. M. Kirka, and P. Nandwana, “Effects of heat treatments on microstructure and properties of Ti-6Al-4V ELI alloy fabricated by electron beam melting (EBM),” *Mater. Sci. Eng. A*, vol. 685, no. January, pp. 417–428, 2017, doi: 10.1016/j.msea.2017.01.019.
[45] Y. Zhai, H. Galarraga, and D. A. Lados, “Microstructure Evolution, Tensile Properties, and Fatigue Damage Mechanisms in Ti-6Al-4V Alloys Fabricated by Two Additive Manufacturing Techniques,” *Procedia Eng.*, vol. 114, pp. 658–666, 2015, doi: 10.1016/j.proeng.2015.08.007.
[46] Y. K. Kim, S. H. Park, Y. J. Kim, B. Almangour, and K. A. Lee, “Effect of Stress Relieving Heat Treatment on the Microstructure and High-Temperature Compressive Deformation Behavior of Ti-6Al-4V Alloy Manufactured by Selective Laser Melting,” *Metall. Mater. Trans. A Phys. Metall. Mater. Sci.*, vol. 49, no. 11, pp. 5763–5774, 2018, doi: 10.1007/s11661-018-4864-0.
[47] B. Vrancken, L. Thijs, J. P. Kruth, and J. Van Humbeeck, “Heat treatment of Ti6Al4V produced by Selective Laser Melting: Microstructure and mechanical properties,” *J. Alloys Compd.*, vol. 541, pp. 177–185, 2012, doi: 10.1016/j.jallcom.2012.07.022.
[48] J. Cappola *et al.*, “On the Localization of Plastic Strain in Microtextured Regions of Ti-6Al-4V,” *Acta Mater.*, vol. 204, p. 116492, 2021, doi: 10.1016/j.actamat.2020.116492.
[49] D. Zhang *et al.*, “Effect of heat treatment on the tensile behavior of selective laser melted Ti-6Al-4V by in situ X-ray characterization,” *Acta Mater.*, vol. 189, pp. 93–104, 2020, doi:

10.1016/j.actamat.2020.03.003.
[50] Y. S. J. Yoo, T. A. Book, M. D. Sangid, and J. Kacher, “Identifying strain localization and dislocation processes in fatigued Inconel 718 manufactured from selective laser melting,” *Mater. Sci. Eng. A*, vol. 724, no. March, pp. 444–451, 2018, doi: 10.1016/j.msea.2018.03.127.
[51] A. J. Wilkinson and T. Ben Britton, “Strains, planes, and EBSD in materials science,” *Mater. Today*, vol. 15, no. 9, pp. 366–376, 2012, doi: 10.1016/S1369-7021(12)70163-3.
[52] S. Villert, C. Maurice, C. Wyon, and R. Fortunier, “Accuracy assessment of elastic strain measurement by EBSD,” *J. Microsc.*, vol. 233, no. 2, pp. 290–301, 2009, doi: 10.1111/j.1365-2818.2009.03120.x.
[53] M. D. Vaudin, Y. B. Gerbig, S. J. Stranick, and R. F. Cook, “Comparison of nanoscale measurements of strain and stress using electron back scattered diffraction and confocal Raman microscopy,” *Appl. Phys. Lett.*, vol. 93, no. 19, 2008, doi: 10.1063/1.3026542.
[54] M. D. Vaudin, G. Stan, Y. B. Gerbig, and R. F. Cook, “High resolution surface morphology measurements using EBSD cross-correlation techniques and AFM,” *Ultramicroscopy*, vol. 111, no. 8, pp. 1206–1213, 2011, doi: 10.1016/j.ultramic.2011.01.039.
[55] G. Miyamoto, A. Shibata, T. Maki, and T. Furuhara, “Precise measurement of strain accommodation in austenite matrix surrounding martensite in ferrous alloys by electron backscatter diffraction analysis,” *Acta Mater.*, vol. 57, no. 4, pp. 1120–1131, 2009, doi: 10.1016/j.actamat.2008.10.050.
[56] V. Thampy *et al.*, “Subsurface Cooling Rates and Microstructural Response during Laser Based Metal Additive Manufacturing,” *Sci. Rep.*, vol. 10, no. 1, pp. 1–9, 2020, doi: 10.1038/s41598-020-58598-z.
[57] G. Nolze and R. Hielscher, “Orientations – perfectly colored,” pp. 1786–1802, 2016, doi: 10.1107/S1600576716012942.
[58] F. Bachmann, R. Hielscher, and H. Schaeben, “Texture analysis with MTEX- Free and open source software toolbox,” *Solid State Phenom.*, vol. 160, pp. 63–68, 2010, doi: 10.4028/www.scientific.net/SSP.160.63.
[59] R. Hielscher, C. B. Silbermann, E. Schmidl, and J. Ihlemann, “Denoising of crystal orientation maps research papers,” pp. 984–996, 2019, doi: 10.1107/S1600576719009075.
[60] D. Fullwood and H. Lanson, “OpenXY.” Salt Lake City, 2015.
[61] K. A. Small, Z. Clayburn, R. DeMott, S. Primig, D. Fullwood, and M. L. Taheri, “Interplay of dislocation substructure and elastic strain evolution in additively manufactured Inconel 625,” *Mater. Sci. Eng. A*, vol. 785, no. January, p. 139380, 2020, doi: 10.1016/j.msea.2020.139380.
[62] R. Shi and Y. Wang, “Variant selection during α precipitation in Ti-6Al-4V under the influence of local stress - A simulation study,” *Acta Mater.*, vol. 61, no. 16, pp. 6006–6024, 2013, doi: 10.1016/j.actamat.2013.06.042.
[63] A. M. Stapleton, S. L. Raghunathan, I. Bantounas, H. J. Stone, T. C. Lindley, and D. Dye, “Evolution of lattice strain in Ti-6Al-4V during tensile loading at room temperature,” *Acta Mater.*, vol. 56, no. 20, pp. 6186–6196, 2008, doi: 10.1016/j.actamat.2008.08.030.
[64] T. W. Heo and L. Q. Chen, “Phase-field modeling of displacive phase transformations in elastically anisotropic and inhomogeneous polycrystals,” *Acta Mater.*, vol. 76, pp. 68–81, 2014, doi: 10.1016/j.actamat.2014.05.014.
[65] S. Bhattacharyya, T. W. Heo, K. Chang, and L. Q. Chen, “A spectral iterative method for the computation of effective properties of elastically inhomogeneous polycrystals,” *Commun. Comput. Phys.*, vol. 11, no. 3, pp. 726–738, 2012, doi: 10.4208/cicp.290610.060411a.
[66] S. Bhattacharyya, T. W. Heo, K. Chang, and L. Q. Chen, “A phase-field model of stress effect on grain boundary migration,” *Model. Simul. Mater. Sci. Eng.*, vol. 19, no. 3, 2011, doi: 10.1088/0965-0393/19/3/035002.
[67] R. Shi, S. Khairallah, T. W. Heo, M. Rolchigo, J. T. McKeown, and M. J. Matthews, “Integrated

Simulation Framework for Additively Manufactured Ti-6Al-4V: Melt Pool Dynamics, Microstructure, Solid-State Phase Transformation, and Microelastic Response," *Jom*, vol. 71, no. 10, pp. 3640–3655, 2019, doi: 10.1007/s11837-019-03618-1.

[68] T. W. Heo *et al.*, "A mesoscopic digital twin that bridges length and time scales for control of additively manufactured metal microstructures," *JPhys Mater.*, vol. 4, no. 3, 2021, doi: 10.1088/2515-7639/abeef8.

[69] M. Ohring, "HOW ENGINEERING MATERIALS ARE STRENGTHENED AND TOUGHENED," *Eng. Mater. Sci.*, pp. 431–500, Jan. 1995, doi: 10.1016/B978-012524995-9/50033-7.

[70] K. A. Small, I. D. McCue, K. S. Johnston, I. Donaldson, and M. L. Taheri, "Precision Modification of Microstructure and Properties Through Laser Engraving," *Jom*, vol. 73, no. 12, pp. 4211–4220, 2021, doi: 10.1007/s11837-021-04959-6.

[71] J. W. Christian, G. B. Olson, and M. Cohen, "Classification of Displacive Transformations : What is a Martensitic Transformation ?," *J. Phys. IV*, vol. 5, no. December, 1995, doi: 10.1051/jp4:1995801.

[72] R. Shi, S. A. Khairallah, T. T. Roehling, T. W. Heo, J. T. McKeown, and M. J. Matthews, "Microstructural control in metal laser powder bed fusion additive manufacturing using laser beam shaping strategy," *Acta Mater.*, vol. 184, pp. 284–305, 2020, doi: 10.1016/j.actamat.2019.11.053.

[73] S. Wei, J. Kim, and C. C. Tasan, "In-situ investigation of plasticity in a Ti-Al-V-Fe (α+β) alloy: Slip mechanisms, strain localization, and partitioning," *Int. J. Plast.*, vol. 148, no. August 2021, p. 103131, 2022, doi: 10.1016/j.ijplas.2021.103131.

[74] C. E. Andrews, "Data for: Codependency of strain and phase evolution of additively manufactured Ti-6Al-4V." Mendeley Data, p. v3, 2022, doi: 10.17632/zzdjysc98c.2.

Supplementary

Table S.1: L-PBF Manufacturing Parameters

Manufacturing Parameter	Value [unit]
Shielding gas	Argon
Build plate material	Stainless steel
Layer thickness	20 [um]
Laser power	200 [W]
Spot size	55 [um]
Build rate	7.13 [cm^3/hr]
Total build volume	14.25 [cm^3]